

# Strain-hardening characteristics of ferrite layers in pearlite microstructure

メタデータ	言語: eng 出版者: 公開日: 2018-06-08 キーワード (Ja): キーワード (En): 作成者: メールアドレス: 所属:
URL	<a href="https://doi.org/10.24517/00049670">https://doi.org/10.24517/00049670</a>

This work is licensed under a Creative Commons Attribution-NonCommercial-ShareAlike 3.0 International License.



# **Strain-hardening characteristics of ferrite layers in pearlite microstructure**

Y. Yasuda<sup>a\*</sup>, T. Ohashi<sup>b</sup>, T. Shimokawa<sup>a</sup> and T. Niiyama<sup>a</sup>

<sup>a</sup>*Institute of Science and Engineering, Kanazawa University, Kanazawa, Japan;*

<sup>b</sup>*Kitami Institute of Technology, Kitami, Japan*

e-mail for the \*corresponding author: [yasuda@se.kanazawa-u.ac.jp](mailto:yasuda@se.kanazawa-u.ac.jp)

## **Strain-hardening characteristics of ferrite layers in pearlite microstructure**

Strain hardening of ferrite layers in pearlite microstructures plays a crucial role in the stability of elasto-plastic deformation of pearlite. The effects of layer thickness, crystal orientation relationship and loading direction on the strain-hardening characteristics of the ferrite layers were studied by crystal plasticity analysis. The results show that the strain-hardening rate increases in the ferrite layers with small thickness, whereas at the same thickness, the strain-hardening rate varies depending on the loading direction and crystal orientation relationship. When the Schmid factors and mean-free paths of the activated systems are small and short, the strain-hardening rate tends to be high. The ferrite layer exhibits a remarkably high strain-hardening rate when slip systems are sequentially activated with the increase of deformation.

Keywords: Crystal plasticity analysis; Pearlite; Ferrite; Strain-hardening characteristics; Size effect; Strain-hardening anisotropy

### **Introduction**

Pearlite steels have been widely used as structural materials since they exhibit both high strength and a certain extent of ductility<sup>1-6</sup>. These superior properties arise from the pearlite's microstructure, which comprises ferrite and cementite layers, alternately arranged within submicron intervals. However, the mechanism that leads to these properties, particularly ductility, has not been fully understood yet.

A recent elasto-plasticity analysis<sup>7</sup>) showed that the high strain-hardening ability of ferrite layers in pearlite suppresses the localization of plastic deformation in cementite layers, and then stabilizes elasto-plastic deformation of pearlite phase. This suggests that the strain hardening of the ferrite layers in pearlite microstructures plays a crucial role to improve the ductility of pearlite steels. Hence, revealing the dependence of the strain-hardening rate of the ferrite layers on the characteristic lengths of pearlite

microstructures leads to elucidation of the mechanism resulting in the ductility of pearlite steels.

Strain gradient crystal plasticity analysis<sup>8,9)</sup> is a powerful technique to investigate the influence of the characteristic length of the microstructures in pearlite steels on the strain-hardening rate of the ferrite layers as it can treat the size effect of the microstructures by introducing the characteristic length in constitutive equations. Indeed, in our previous study that we introduced lengths related to the ferrite layer thickness to the constitutive equations, the strain-hardening rate of the ferrite layers depends on the layer thickness under a uniaxial tensile deformation condition for a specific crystal orientation<sup>10,11)</sup>. This dependence comes from the accumulation of dislocations; the thin ferrite layers lead to accumulation of dislocations which make further plastic deformation difficult. However, under different deformation conditions, the influence of the layer thickness on the strain-hardening rate is unclear because the controlling factors of the strain hardening rate such as the Schmid factors, mean-free path (MFP) of dislocations, and number of active slip systems, vary according to the loading conditions.

In this paper, to specify the controlling factors for the increase of strain-hardening rate of the ferrite layers in pearlite microstructures, we systematically investigate the strain-hardening rate of the ferrite layers with different layer thickness under the various loading directions and relative crystal orientation relationships between ferrite and cementite layers by strain gradient crystal plasticity analysis. As for the crystal orientation relationship between ferrite and cementite layer, the Bagaryatsky<sup>12)</sup> and Pitsch-Petch<sup>13,14)</sup> relationship are used, the layer thicknesses are 50 nm and 500 nm, and ten loading directions are studied; 40 kinds of analyses are performed as a whole. From the analysis, we clarify that a parameter consisting of the

characteristic length of ferrite layers and the Schmid factors mainly contribute to the strain-hardening rate. Moreover, we also demonstrated that the sequential activation of the slip systems in ferrite layers can result in a remarkable increase of the strain-hardening rate.

### Strain gradient crystal plasticity analysis for a layered microstructure

In this section, we describe our developed models of the critical resolved shear stress (CRSS) and MFP of moving dislocations to express the plastic deformations for a ferrite layer sandwiched by cementite layers in pearlite microstructures in the crystal plasticity analyses. The development of the present model is based on our crystal plasticity model<sup>8,9)</sup>. In this study, twenty-four slip systems of the  $\{110\}\langle 111\rangle$  and  $\{112\}\langle 111\rangle$  family are considered in the ferrite phase.

Before describing the CRSS and MFP models, we present the elasto-plastic constitutive equations for the slip deformations based on the infinitesimal deformation theory<sup>15)</sup> as follows:

$$\dot{\sigma}_{ij} = \left[ S_{ijkl}^e + \sum_n \sum_m \left\{ h^{(nm)} \right\}^{-1} P_{ij}^{(n)} P_{kl}^{(m)} \right]^{-1} \dot{\varepsilon}_{kl}, \quad (1)$$

where  $\sigma_{ij}$ ,  $\varepsilon_{kl}$ ,  $S_{ijkl}^e$ ,  $P_{ij}^{(n)}$  and  $h^{(nm)}$  are the stress tensor, total strain tensor, the elastic compliance, the Schmid tensor, and a strain-hardening parameter, respectively. The bracketed superscript represents the number which is sequentially assigned to each slip system. The indexes  $n$  and  $m$  are the indexes of a slip system. The summation  $\sum_m$  is made over the active slip systems. The Schmid tensor  $P_{ij}^{(n)}$  is defined by  $(v_i^{(n)} b_j^{(n)} + v_j^{(n)} b_i^{(n)})/2$  where  $v_i^{(n)}$  and  $b_i^{(n)}$  are the slip plane normal vector and slip direction vector, respectively. The strain-hardening parameter  $h^{(nm)}$  determined by CRSS (the detail of the parameter will be described in Eq. (6)) represents the

instantaneous influence of plastic shear strain on  $m$ -th slip system on the increment of the CRSS for  $n$ -th slip system as follows<sup>16</sup>:

$$\dot{\theta}^{(n)} = \sum_m h^{(nm)} \dot{\gamma}^{(m)}, \quad (2)$$

where  $\theta^{(n)}$  and  $\gamma^{(m)}$  represent the CRSS and the plastic shear strain.

First, we describe the CRSS for slip system  $n$  for ferrite layers in pearlite microstructure as follows:

$$\theta^{(n)} = \theta_0 + \sum_m \Omega^{(nm)} a \mu \tilde{b} \sqrt{\rho_s^{(m)}} + C_T \frac{\mu \tilde{b}}{\hat{d}^{(n)}}. \quad (3)$$

This is an extended Bailey–Hirsch type model<sup>9</sup>. The first term in the right hand side stands for lattice-friction stress for moving dislocations and the second term defines slip resistance of statistically stored (SS) dislocations on 24 slip systems against moving ones on the slip system  $n$ .  $\theta_0$  and  $\mu$ ,  $\tilde{b}$ ,  $\rho_s^{(m)}$  are the lattice-friction stress, the elastic shear modulus, the magnitude of the Burgers vector, and the density of the SS dislocations.  $a$  is a numerical coefficient, and  $\Omega^{(nm)}$  is a matrix defining the strength of interaction between the slip systems  $n$  and  $m$ . The third term in the right-hand side represents the dislocation-multiplication stress from the Frank-Read (FR) source. This term is necessary for the microstructure plasticity because the dislocation-multiplication stress cannot be neglected against the lattice-friction stress given by the second term due to the geometrical restriction by plane defects for the dislocation bow-out<sup>9</sup>. Therefore, the third term can have a characteristic length  $\hat{d}^{(n)}$  related to the pearlite microstructure.  $\hat{d}^{(n)}$  is the shortest distance between the layers on the slip plane of the slip system  $n$ , as shown in Fig. 1(a). In the case that the FR source is positioned at the centre of the slip plane, the dislocation-multiplication stress is  $2\mu b/\hat{d}^{(n)}$  when the FR source is parallel to the interface ( $C_T = 2$ ), or  $3\mu b/\hat{d}^{(n)}$  when the FR source is perpendicular to the interface ( $C_T = 3$ ), as shown in Fig. 1(a).

Second, the MFP for ferrite layers in the pearlite microstructure is described. MFP  $L^{(n)}$  represents the distance within which a dislocation moving on the slip plane is trapped by obstacles. The MFP  $L^{(n)}$  is defined by the following equation<sup>16)</sup>:

$$\dot{\rho}_S^{(n)} = \frac{c\dot{\gamma}^{(n)}}{\tilde{b}L^{(n)}}, \quad (4)$$

where  $c$  is a constant. Generally, dislocations accumulated in materials are considered to be obstacles for the movement of other dislocations. In our crystal plasticity analysis, these obstacles are represented by SS dislocations and geometrically necessary (GN) dislocations which are evaluated by the plastic-strain gradient. The MFP by dislocation accumulation is estimated by the first term in the right-hand side of the following Eq. (5). In the lamellar microstructure of pearlite, the interfaces between the ferrite and cementite layers can also be regarded as obstacles. The MFP by the interface is modelled as shown in Fig. 1(b). Let us consider a situation wherein a dislocation on a slip plane enters the interface. The screw component of the impinged dislocation can easily change its position by a cross slip along the interface but for the edge component, a climb motion along the interface is required to change its position. Therefore, the edge components stacked at the interface become an obstacle for the motion of subsequent dislocations on the same slip plane approaching the interface. We assume that the slip system on the slip plane cannot be activated when the sum of the edge components of impinged dislocations at the interface becomes equal to  $\beta^*\|\mathbf{b}\|$ . As shown in Fig. 1(b), when a dislocation, with the Burgers vector  $\mathbf{b}$  inclined by  $\theta$  with respect to the direction perpendicular to a layer interface, starts to glide from a dislocation source at the vicinity of the interface and enters the other side interface, the edge component  $b_{\text{edge}} = \|\mathbf{b}\|\cos\theta$  is added to the other side interface. Then, the total distance that dislocations can move on this slip plane, until the sum of  $b_{\text{edge}}$  reaches  $\beta^*\|\mathbf{b}\|$ , is  $\beta^*\hat{d}/\cos\theta$ . This total distance

is equal to  $\beta^* d^{*(n)}$ , where  $d^{*(n)}$  is the distance between the interfaces in the direction of the Burgers vector  $\mathbf{b}$ , (Fig. 1). Consequently,  $\beta^* d^{*(n)}$  is the MFP when the interfaces act as obstacles. In our crystal plasticity analysis, the smaller one of the MFP by dislocation accumulation and the MFP by interfaces is defined as the MFP of ferrite layers in pearlite microstructures. Herein, the MFP is mathematically expressed as

$$L^{(n)} = \min \left( \frac{c^*}{\sqrt{\sum_{m=1}^{24} \omega^{(nm)} (\rho_S^{(m)} + \|\rho_G^{(m)}\|)}}, \beta^* d^{*(n)} \right). \quad (5)$$

$\omega^{(nm)}$  and  $c^*$  are the weight matrix and a constant, respectively.  $\|\rho_G^{(m)}\|$  is the density norm of the GN dislocations.

Finally, we consider the controlling factors for the high strain-hardening rate of ferrite layers in pearlite microstructures. Eq. (1) clearly shows that to increase the strain-hardening rate, a large  $h^{(nm)}$ , a large number of active slip systems (multiple slip) and a small  $P_{ij}^{(n)}$  are required. The strain-hardening parameter  $h^{(nm)}$  can be derived by Eq. (2), (3) and (4) as follows:

$$h^{(nm)} = \frac{\Omega^{(nm)} a \mu c}{2L^{(m)} \sqrt{\rho_S^{(m)}}}. \quad (6)$$

Eq. (6) shows that to increase  $h^{(nm)}$ , the MFP  $L^{(m)}$  should be short. Hence, it can be inferred that controlling factors for the high strain hardening rate are a multiple slip, a small Schmid factor  $P_{ij}^{(n)}$  and a short MFP  $L^{(m)}$ .

### Analysis model

Fig. 2(a) shows the model of the pearlite microstructure configuration, expressed as  $\text{Fe}_3\text{C}/\alpha/\text{Fe}_3\text{C}$  wherein the ferrite layer  $\alpha$  is sandwiched between two  $\text{Fe}_3\text{C}$  cementite layers. The dimensions of the layered-structure considered are  $5l$ ,  $l$  and  $5l$  in the  $x_1$ ,  $x_2$

and  $x_3$  directions, respectively. The ferrite layer thickness  $d$  is  $5l/7$ . To investigate the dependence of the strain-hardening rate on the thickness of the ferrite layer, two cases with  $d = 50$  nm and 500 nm (as observed in the experiments<sup>1,2</sup>) are considered.

To clarify the effect of the controlling factors on the strain-hardening characteristics of ferrite layers, we simplify the material behaviour as follows: (1) the ferrite and cementite layers have the same elastic modulus and Poisson's ratio ( $E = 200$  GPa and  $\nu = 0.3$ ) and (2) the cementite layers deform only elastically. This simplification allows us to extract the contribution of geometrical factors, such as layer thickness, slip systems, and so on, to the RSS of each slip system in ferrite layer. The plastic deformation of  $\alpha$  is expressed by the constitutive equations described in the previous section.

The material constants and numerical coefficients are the same as previous studies<sup>10,11</sup>) and summarized in Table 1. The initial total dislocation density  $\rho_0$  in the ferrite layer is set to  $10^{11} \text{ m}^{-2}$ . Because no GN dislocation density appears until plastic deformations are triggered, and the initial SS dislocation density of each slip system is  $\rho_0/24$ , i.e.  $\rho_S^{(m)} = 4.17 \times 10^9 \text{ m}^{-2}$ .  $\tilde{b}$  and  $\theta_0$  are  $2.48 \times 10^{-10} \text{ m}$  and 23 MPa, respectively. We assume an isotropic type interaction matrix of  $\Omega^{(nm)} \cong 1$  in Eq. (3) and this means the hardening in the ferrite phase is close to the isotropic one. For the weight matrix  $\omega^{(nm)}$ , we use 0 for the diagonal component and 1 for the off-diagonal component. The constants  $a$ ,  $C_T$ ,  $c$ ,  $c^*$  and  $\beta^*$  are 0.1, 3, 2, 20 and 1, respectively.

The crystal orientation relationship between the ferrite and cementite layers is determined from the Bagaryatsky<sup>12)</sup> or Pitsch-Petch<sup>13,14)</sup> relationships. For the Bagaryatsky relationship, the conditions  $(001)_{\text{Fe}_3\text{C}} // (11-2)_\alpha$  and  $[010]_{\text{Fe}_3\text{C}} // [111]_\alpha$  hold. The subscript represents the layer name. In the Pitsch-Petch relationship,  $(001)_{\text{Fe}_3\text{C}} // (-2-15)_\alpha$  and  $[010]_{\text{Fe}_3\text{C}} 2.6^\circ$  from  $[131]_\alpha$  hold; however the small deviation

has been neglected and the orientation relationship has been regarded as  $[010]_{\text{Fe}_3\text{C}}//[131]_{\alpha}$  for simplicity.

Previous experimental results showed that  $\alpha$  exhibits  $\langle 110 \rangle$  texture along the drawing direction<sup>3</sup>); hence, in both Bagaryatsky and Pitsch–Petch relationships, the  $\langle 110 \rangle$  direction has been initially set as the  $x_1$  direction that corresponds to the loading direction. The detailed crystal orientation of the  $\alpha$  layer is shown in Fig. 2(b) for the Bagaryatsky relationship and in Fig. 2(c) for the Pitsch–Petch relationship. To investigate the influence of the loading direction on the strain-hardening characteristics of  $\alpha$ , the  $\langle 110 \rangle$  direction of  $\alpha$  of an angle  $\varphi$  is rotated around the  $x_2$ -axis from the initial crystal orientations at intervals of  $10^\circ$ . To simulate tensile loading conditions, a uniform tensile displacement is imposed on the surface nodes at  $x_1 = 5l$ , whereas the displacement of the nodes on the opposite surface is constrained along the  $x_1$  direction (Fig. 2(a)). Free boundary condition is adapted for the other surfaces. The total number of finite elements is 6272.

## Results

Fig. 3 shows the stress–strain curves of the ferrite layer ( $\alpha$ ) in the  $\text{Fe}_3\text{C}/\alpha/\text{Fe}_3\text{C}$  model. The stress and plastic strain are averaged over all ferrite elements in the model. Circles and square symbols in the figure represent the results relative to the ferrite layer thickness of 500 and 50 nm, respectively. The open and closed symbols indicate the results obtained using the Bagaryatsky and Pitsch–Petch relationships, respectively. The thick line represents the stress–strain curve of the virtual ferrite (ferrite 5) with a high strain-hardening characteristic expressed by the modified Swift equation  $\sigma = a(b + \varepsilon_p)^n + c$  in the classical elasto-plasticity analysis<sup>7</sup>). This strain-hardening characteristic of the virtual ferrite can stabilize the plastic instability of the cementite layer. The thin lines are obtained from using the modified Swift equation employed to fit the obtained results.

For both Bagaryatsky and Pitsch–Petch relationships, the strain-hardening rate of ferrite layers with small thickness is higher than that observed in the large thickness model.

The crystal orientation relationships influence the degree of the layer-thickness dependence of the strain-hardening rate. For a large thickness of 500 nm, the strain-hardening rate in the Bagaryatsky relationship is higher than that in the Pitsch–Petch relationship. For a small ferrite layer thickness (50 nm), the Pitsch–Petch relationship shows a higher strain-hardening rate than that of the Bagaryatsky relationship.

Subsequently, the loading-direction dependence of the strain-hardening rate is examined. Fig. 4 shows the relationship between the strain-hardening rate at plastic strain 0.03 and the loading direction  $\varphi$ . The strain-hardening rates are estimated by fitting the modified Swift equation shown in Fig. 3. For the same loading direction, the strain-hardening rates of the 50 nm thickness are higher than that of the 500 nm thickness; hence, the layer-thickness dependence of the strain-hardening rate confirmed in Fig. 3 holds in all loading directions. The loading-direction dependence of the strain-hardening rate is clearly observed when the loading direction  $\varphi$  is larger than  $60^\circ$ . The strain-hardening rates with  $\varphi \geq 60^\circ$  shows higher than that the smaller  $\varphi$ . Interestingly, although the 500 nm thickness of the Bagaryatsky relationship with  $\varphi \geq 60^\circ$ , the strain-hardening rates take almost the same value of the virtual ferrite (ferrite5)<sup>7</sup> that can suppress the plastic instability of the cementite layer. Consequently, strain-hardening anisotropy clearly appears in ferrite layers in pearlite microstructures.

## Discussions

Why does the strain-hardening rate depend on the layer thickness, crystal orientation, and loading direction as shown in Figs. 3 and 4? We investigate the loading-direction dependence of the strain-hardening rate by focusing on the presumed controlling factors: the number of active slip systems, the Schmid factor, and the MFP

as mentioned in Sec. 2. Fig. 5 shows the number of active slip systems, average Schmid factor and average MFP for each  $\varphi$  when the plastic strain is 0.03. The average Schmid factor and MFP are calculated using the SS dislocation densities of active slip systems as follows:

$$\overline{P}_{11} = \frac{\sum_n \rho_{SS,0.03}^{(n)} P_{11}^{(n)}}{\sum_n \rho_{SS,0.03}^{(n)}}, \quad \overline{L} = \frac{\sum_n \rho_{SS,0.03}^{(n)} L_{0.03}^{(n)}}{\sum_n \rho_{SS,0.03}^{(n)}}. \quad (7)$$

The subscript 0.03 indicates the plastic strain value.

First, we consider the dependence of layer thickness on strain hardening rate. From Fig. 5, one can easily find that  $\overline{L}$  exhibits remarkable dependence of layer thicknesses (Fig. 5(c)), in contrast with the number of active slip systems and average Schmid tensor components (Figs. 5(a) and (b)). This remarkable dependence is originated from the fact that MFPs of most slip systems are determined by  $\beta^* d^{*(n)}$  in Eq. (5). Therefore, it is found that the layer thickness dependence of the strain-hardening rate in Figs. 3 and 4 is mainly caused by the MFP.

Second, we consider the dependence of the crystal orientation between ferrite and cementite for  $\varphi=0$  with the same layer thickness as shown in Fig. 3. In terms of the Schmid factor, one can find that the Schmid factor of the model with the Pitsch–Petch relationship is larger than that of the model with the Bagaryatsky relationship for both 50 and 500 nm layer thickness. If the strain hardening rate is determined by only the Schmid factors, the rate of the Pitsch–Petch relationship would be smaller than that of the Bagaryatsky relationship. However, this expectation is inconsistent with the trend shown in Fig. 3. In this case, the dominant controlling factor is the number of active slip systems. As shown in Fig. 5(a), the hierarchical relation of the number of slip systems of the Pitsch–Petch and the Bagaryatsky relationship is inverted depending on the layer thicknesses. This inversion phenomenon is the origin of the dependence of the crystal

orientation in Fig. 3. The change of the number of active slip systems is mainly due to the increase of the dislocation-multiplication stress, described by the third term on the right-hand side of Eq. (3), with decrease in the ferrite layer thickness regardless of the Schmid factor. The slip system with the largest Schmid factor is not necessarily activated firstly or not activated in ferrite layers if the increase of the CRSS is higher than that for other slip systems.

Third, we consider the dependence of the loading-direction. The loading-direction dependence of the average Schmid factor and MFP in Figs. 5(b) and (c) show good correlations with the strain-hardening rate in Fig. 4. For  $\varphi \geq 60^\circ$ , the average Schmid factor and average MFP, except for the 50 nm layer of the Pitsch–Petch relationship, have smaller values than in the region wherein  $\varphi < 60^\circ$ ; therefore, the strain-hardening rate becomes increases.

To investigate the contribution of the Schmid factor and the MFP to the strain-hardening rate, we derive an expression of the strain-hardening parameter  $h^{(nm)}$  (see Appendix A) by regarding the actual multiple slip phenomena as the simple single slip phenomena with the Schmid factor  $P_{11}$  and the MFP  $L$  in ferrite layers. Eq. (A3) shows that the strain-hardening parameter increases with  $1/\sqrt{LP_{11}^3}$ . Fig. 6 shows the relationship between the strain-hardening rate and  $1/\sqrt{LP_{11}^3}$ . The average Schmid factor  $\bar{P}_{11}$  and the average MFP  $\bar{L}$  in Eq. (7) are used for  $P_{11}$  and  $L$ , respectively. The strain-hardening rate estimated by the crystal plasticity analysis and  $1/\sqrt{\bar{L}\bar{P}_{11}^3}$  derived by assuming the simple slip system show a good positive correlation (Fig. 6). Consequently, the controlling factors for the high strain-hardening rate are a small Schmid factor and a short MFP. To activate slip systems with small Schmid factors, the CRSS for slip systems with larger Schmid factors must be larger than those slip systems.

Our crystal plasticity analysis shows the possibility of controlling the CRSS for each slip systems by designing the lamellar thickness, crystal orientation relationship and loading direction.

In addition to the above controlling factors, we have a chance to find a further factor which can dramatically improve the strain-hardening rate because the highest strain-hardening rate in Fig. 6 ( $\varphi = 80^\circ$  for Bagaryatsky relationship with  $d=50$  nm) deviates greatly from the positive correlation relation discussed above. To examine this reason, the evolution of active slip systems has been monitored in the loading tests simulated for  $\varphi = 80^\circ$  and  $90^\circ$  for the Bagaryatsky relationship with  $d = 50$  nm corresponding to the black and white arrows in Fig. 6. Fig. 7 shows the change of SS dislocation densities of the active slip systems during plastic deformation. The SS dislocation density  $\rho_s^{(n)}$  represents an activity of slip system  $n$ . For  $\varphi = 90^\circ$ , the activations of the slip systems mainly occur during the initial stage of plastic deformations. For  $\varphi = 80^\circ$ , the slip systems with a small Schmid factor are sequentially activated with the increase of the external load: the increase of the CRSS of the first-activated sys23 with the larger Schmid factor of 0.38 and the initial MFP of 106 nm activates the sys24 with the smaller Schmid factor of 0.32 and the same initial MFP of 106 nm and other slip systems with the even smaller Schmid factor and the shorter MFP. The comparison of the activations of slip systems for  $\varphi = 90^\circ$  and  $\varphi = 80^\circ$  suggests that the sequential activation of the slip systems with a small Schmid factor in ferrite layers can result in a remarkably high strain-hardening rate. The simultaneous activation of multi slip system or sequential activation of slip system is realized by developments of the MFP for each slip system during deformation because the developments of the MFP influence the developments of the CRSS for each slip system.

Our previous atomic simulations have reported that the influence of the bonding strength of interface on mechanical properties of pearlite steels is important<sup>17)</sup>. To include that, in this study, we introduced the coefficient  $\beta^*$  in the constitutive equation of the MFP. A larger value of  $\beta^*$  means that the interface can absorb larger number of dislocations and makes the MFP larger. That is,  $\beta^*$  relates the MFP and the dislocation absorbing capacity of the interface. The situation with a larger  $\beta^*$  corresponds to a weaker interface strength in the molecular dynamics simulation<sup>17)</sup>. Results of the molecular dynamics simulation show that the cementite layer in pearlite microstructures is inherently brittle if the interface is weak<sup>17)</sup>. Results of our elasto-plastic analysis<sup>7)</sup>, on the other hand, show that the ductility of pearlite steels is largely influenced by the strain-hardening ability of ferrite layers. Higher strain hardening of the ferrite layer suppresses the localization of plastic deformation in the cementite layers. These two results indicate together that the crystal plasticity analysis considering the influence of interface bonding strength and the molecular dynamics analysis reach almost similar conclusion that the interface strength has a significant importance to the ductility of pearlite steels. In addition to this, the role of the interface must play an important role in the dynamic recovery of stored dislocations that is not considered in the present study. Detailed studies on these roles of interfaces in plastic behaviours of pearlite microstructures are left for the future work.

## **Conclusions**

To elucidate the controlling factors controlling increasing the strain-hardening rate of ferrite layers in pearlite microstructures, the influences of layer thickness, crystal orientation relationship and loading direction were investigated by crystal plasticity analysis. The results can be summarised as follows:

- The smaller the mean-free path of dislocations rather than the layer thickness results in the higher the strain-hardening rate.
- The controlling factor increasing the strain-hardening rate is the value consisting of the average mean-free path  $\bar{L}$  and average Schmid factor  $\bar{P}_{11}$  over active slip systems,  $1/\sqrt{\bar{L}\bar{P}_{11}^3}$ .
- Among the ferrite layers with the same thickness, those having active slip systems with smaller Schmid factor showed higher strain-hardening rate.
- The strain-hardening rate of the ferrite layers undergoing a sequential activation of slip systems showed a remarkably high value than that found in ferrite layers whose slip systems are activated all at once.

### Acknowledgements

This research was supported by the Japan Science and Technology Agency under Collaborative Research Based on Industrial Demand ‘Heterogeneous Structure Control: Towards Innovative Development of Metallic Structural Materials’. This research was also supported by MEXT as ‘Exploratory Challenge on Post-K computer’ (Frontiers of Basic Science: Challenging the Limits).

### Appendix A

In the case of a single slip (slip system number is  $n$ ), Eq. (2) becomes  $\dot{\gamma}^{(n)} = \dot{\theta}^{(n)} / h^{(nn)}$ .

By using the following equations,

$$\dot{\epsilon}_{ij}^p = \dot{\gamma}^{(n)} P_{ij}^{(n)}, \quad (\text{A1})$$

$$\dot{\theta}^{(n)} = P_{ij}^{(n)} \dot{\sigma}_{ij}, \quad (\text{A2})$$

we get  $\dot{\epsilon}_{ij}^p = (P_{kl}^{(n)} \dot{\sigma}_{kl} / h^{(nn)}) P_{ij}^{(n)}$ . If we assume a uniaxial stress state, this equation

reduces to

$$\dot{\sigma}_{11} = \frac{h^{(nm)}}{P_{11}^{(n)} P_{11}^{(n)}} \dot{\varepsilon}_{11}^p. \quad (\text{A3})$$

By substituting Eqs. (4), (6) and (A1) into Eq. (A3), we obtain the equation containing the Schmid factor and MFP as follows:

$$\frac{\dot{\sigma}_{11}}{\dot{\varepsilon}_{11}^p} = \frac{\Omega^{(nm)} a \mu \sqrt{c \tilde{b}}}{2 \sqrt{c \dot{\varepsilon}_{11}^p}} \frac{1}{\sqrt{L^{(n)} (P_{11}^{(n)})^3}}. \quad (\text{A4})$$

Therefore, the strain-hardening rate is proportional to  $1/\sqrt{LP_{11}^3}$ .

## References

1. J. D. Embury and R. M. Fisher: 'The structure and properties of drawn pearlite', *Acta Metall.*, 1966, **14**, 147–159.
2. X. Zhang, A. Godfrey, X. Huang, N. Hansen and Q. Liu: 'Microstructure and strengthening mechanisms in cold-drawn pearlitic steel wire', *Acta Mater.*, 2011, **59**, 3422–3430.
3. F. Fang, L. Zhou, X. Hu, X. Zhou, Y. Tu, Z. Xie and J. Jiang: 'Microstructure and mechanical properties of cold-drawn pearlitic wires affect by inherited texture', *Mater. Des.*, 2015, **79**, 60–67.
4. A. R. Marder and B. L. Bramfitt: 'The effect of morphology on the strength of pearlite', *Met. Trans. A*, 1976, **7**, 365–372.
5. Y. Li, D. Raabe, M. Herbig, P. P. Choi, S. Goto, A. Kostka, H. Yarita, C. Borchers and R. Kirchheim: 'Segregation stabilizes nanocrystalline bulk steel with near theoretical strength', *Phys. Review Lett.*, 2014, **113**, 106104.
6. M. Tanaka, Y. Yoshimi, K. Higashida, T. Shimokawa and T. Ohashi: 'A multiscale approach for the deformation mechanism in pearlite microstructure: Experimental measurements of strain distribution using a novel technique of precision markers', *Mater. Sci. Eng. A*, 2014, **590**, 37–43.
7. T. Ohashi, L. Roslan, K. Takahashi, T. Shimokawa, M. Tanaka, K. Higashida: 'A multiscale approach for the deformation mechanism in pearlite microstructure: Numerical evaluation of elasto-plastic deformation in fine lamellar structures', *Mater. Sci. Eng. A*, 2013, **588**, 214–220.
8. T. Ohashi: 'Crystal plasticity analysis of dislocation emission from micro voids', *Int. J. Plasticity*, 2005, **21**, 2071–2088.

9. T. Ohashi, M. Kawamukai and H. Zbib: 'A multiscale approach for modeling scale-dependent yield stress in polycrystalline metals', *Int. J. Plasticity*, 2007, **23**, 897–914.
10. Y. Yasuda and T. Ohashi: 'Crystal plasticity analyses of scale dependent mechanical properties of ferrite/cementite lamellar structure model in pearlite steel wire with Bagaryatsky or Pitsch–Petch orientation relationship', *ISIJ Int.*, 2016, **56**, 2320–2326.
11. Y. Yasuda and T. Ohashi: 'Crystal plasticity analysis considering dislocations' behavior in ferrite/cementite lamellar structure', *ISIJ Int.*, 2017, **57**, 573–580.
12. Y. A. Bagaryatsky: 'Likely mechanism for the tempering of martensite', *Dokl. Akad. Nauk SSSR*, 1950, **73**, 1161–1164.
13. N. J. Petch: 'The orientation relationships between cementite and  $\alpha$ -iron', *Acta Cryst.*, 1953, **6**, 96.
14. W. Pitsch: 'Der Orientierungszusammenhang zwischen Zementit und Ferrit im Perlit', *Acta Metall.*, 1962, **10**, 79–80.
15. R. Hill: 'Generalized constitutive relations for incremental deformation of metal crystals by multislip', *J. Mech. Phys. Solids*, 1966, **14**, 95–102.
16. T. Ohashi: 'Computer simulation of non-uniform multiple slip in face centered cubic bicrystals', *Trans. Japan Inst. Metals*, 1987, **11**, 906–915.
17. T. Shimokawa, T. Oguro, M. Tanaka, K Higashida and T. Ohashi: 'A multiscale approach for the deformation mechanism in pearlite microstructure: Atomic study of the role of the heterointerface on ductility', *Mater. Sci. Eng. A*, 2014, **598**, 68–76.

Table 1 Material constants of ferrite and cementite used for crystal plasticity analysis.

	Ferrite	Cementite
Elastic constants		
Elastic modulus $E$ , GPa	200	200
Poisson's ratio $\nu$	0.3	0.3
(Elastic shear modulus $\mu$ , GPa)	(76.9)	(76.9)
Magnitude of Burgers vector $b$ , m	$2.48 \times 10^{-10}$	-
Initial dislocation density for each slip system		
SS dislocation, $m^{-2}$	$4.17 \times 10^9$	-
GN dislocation, $m^{-2}$	0	-
Material constants in Eq. (3)		
Lattice friction stress $\theta_0$ , MPa	23	-
Numerical coefficient $a$	0.1	-
Numerical coefficient $C_T$	3	-
Interaction matrix $\mathcal{Q}^{(nm)}$	All components are 1	-
Material constants in Eq. (4)		
Numerical constant $c$	2	-
Material constants in Eq. (5)		
Numerical constant $c^*$	20	-
Numerical constant $\beta^*$	1	-
weight matrix $\omega^{(nm)}$	0 for diagonal components, 1 for off-diagonal components	-

Figure 1. Schematic of (a) dislocation multiplication from the FR source and (b) dislocation accumulation and interaction in ferrite layer. The relative characteristic lengths which relate to dislocation multiplication stress and mean free path (MFP) are  $\hat{d}^{(n)}$  and  $d^{*(n)}$ , respectively.

Figure 2. Schematic of (a) three-layered pearlite model and boundary conditions and (b)(c) initial crystal orientation relationships of ferrite layer for numerical models.  $\langle 110 \rangle$  direction of the ferrite of an angle is rotated  $\varphi$  around the  $x_2$ -axis from the initial crystal orientations. (b) Bagaryatsky and (c) Pitsch–Petch relationships of ferrite layers.

Figure 3. Average stress–strain curves for ferrite layer in the pearlite microstructure models simulated for the loading direction  $\varphi = 0^\circ$  and the virtual ferrite<sup>7)</sup>.

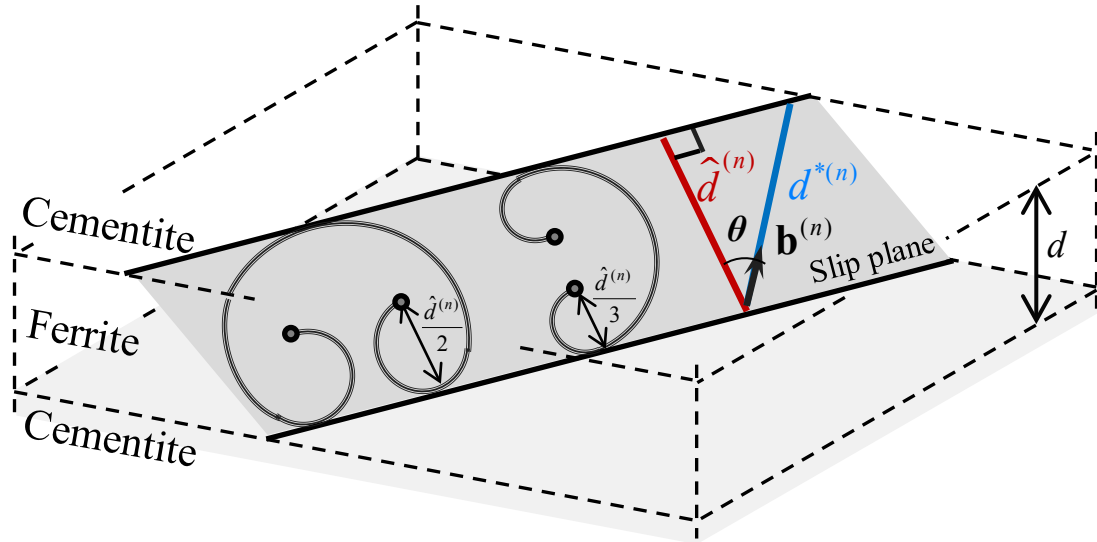
Figure 4. Loading-direction dependence of the strain-hardening rate of ferrite layer in the pearlite microstructure models when the plastic strain is 0.03.

Figure 5. Dependences of (a) number of active slip systems, (b) average Schmid tensor component, and (c) average MFP on strain-hardening rate of ferrite layer in the pearlite microstructure models when the plastic strain is 0.03.

Figure 6 Changes of the strain-hardening rate of ferrite layer in the pearlite microstructure models with  $1/\sqrt{L\bar{P}_{11}^3}$ . The black and white arrows represent the strain-hardening rate of the models with the Bagaryatsky relationship for  $\varphi = 80^\circ$  and  $90^\circ$  when  $d = 50$  nm, respectively.

Figure 7. Average SS dislocation density-strain curves for ferrite layer in the pearlite microstructure models with  $d = 50$  nm. (a)  $\varphi = 90^\circ$  and (b)  $\varphi = 80^\circ$ . Crystal orientation relationship is Bagaryatsky. sys10, 11, 18, 23 and 24 indicate  $(2\ 1\ 1)$   $[-1\ 1\ 1]$ ,  $(1\ 1\ 0)$   $[-1\ 1\ 1]$ ,  $(1\ 1\ 2)$   $[1\ 1\ -1]$ ,  $(1\ 1\ 0)$   $[1\ -1\ 1]$  and  $(1\ 2\ 1)$   $[1\ -1\ 1]$  slip systems, respectively. Numbers in the neighbour bracket show Schmid tensor component and MFP of the slip system, respectively.

(a)



(b)

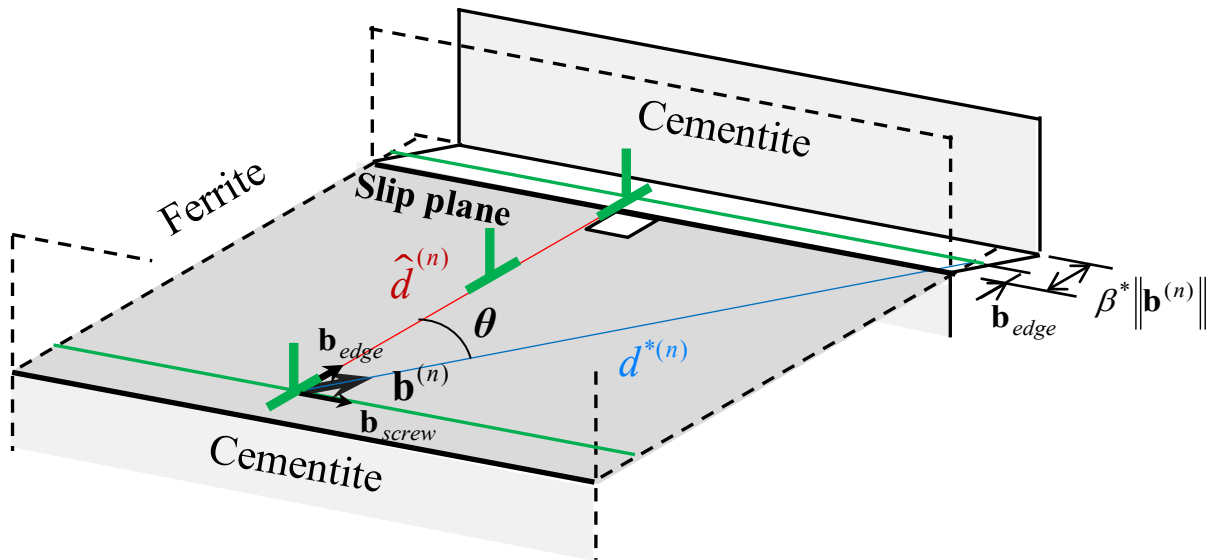
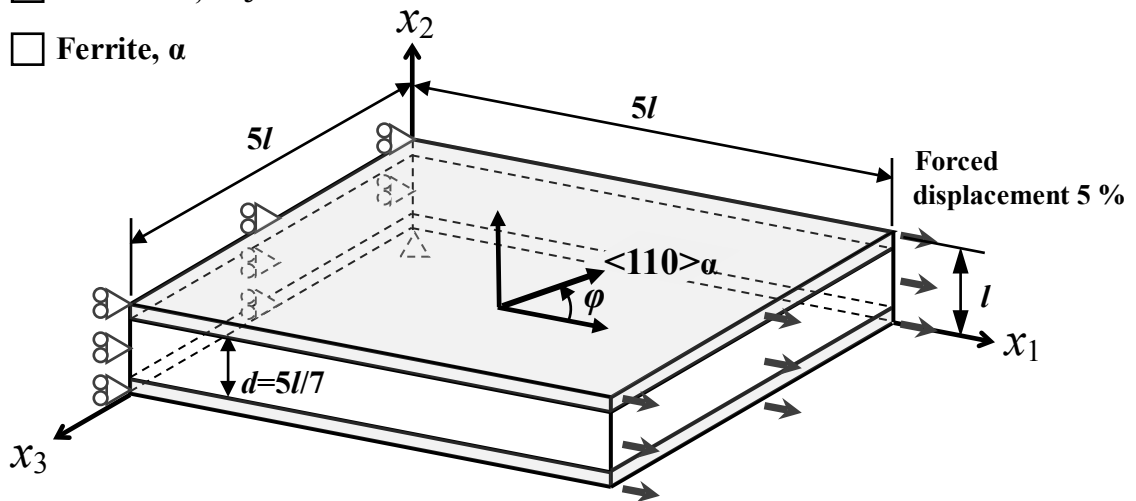


Fig. 1 Schematic of (a) dislocation multiplication from the FR source and (b) dislocation accumulation and interaction in ferrite layer. The relative characteristic lengths which relate to dislocation multiplication stress and mean free path (MFP) are  $\hat{d}^{(n)}$  and  $d^{*(n)}$ , respectively.

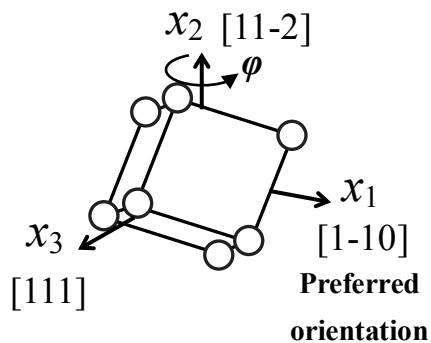
(a)

□ Cementite,  $\text{Fe}_3\text{C}$

□ Ferrite,  $\alpha$



(b)



(c)

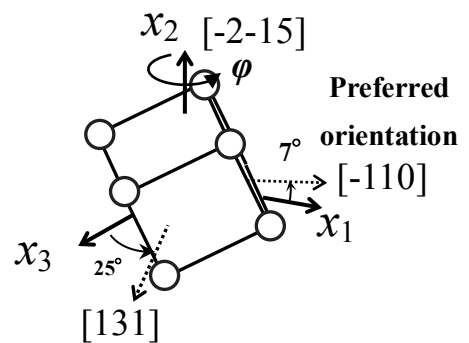


Fig. 2 Schematic of (a) three-layered pearlite model and boundary conditions and (b)(c) initial crystal orientation relationships of ferrite layer for numerical models.  $\langle 110 \rangle$  direction of the ferrite of an angle is rotated  $\varphi$  around the  $x_2$ -axis from the initial crystal orientations. (b) Bagaryatsky and (c) Pitsch-Petch relationships of ferrite layers.

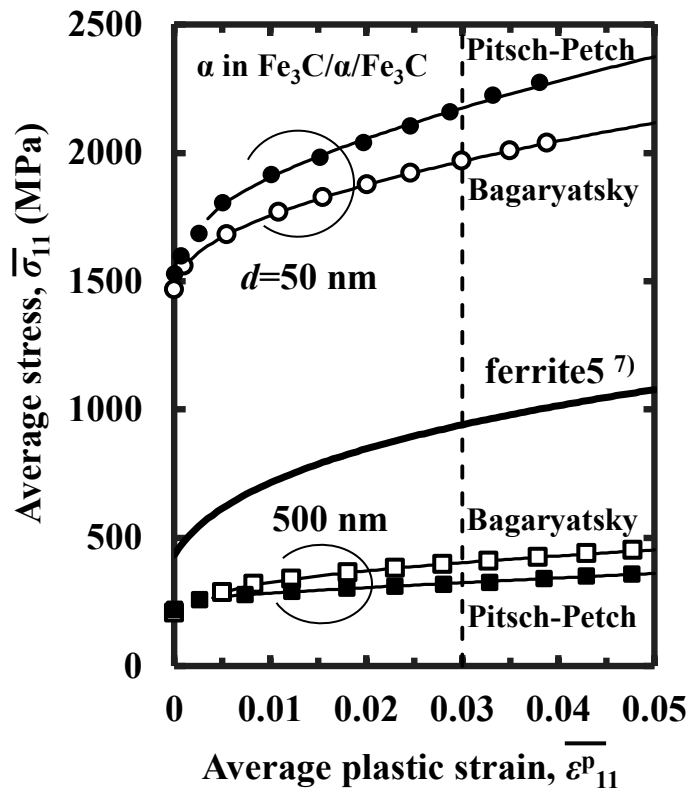


Fig. 3 Average stress–strain curves for ferrite layer in the pearlite microstructure models simulated for the loading direction  $\varphi = 0^\circ$  and the virtual ferrite<sup>7)</sup>.

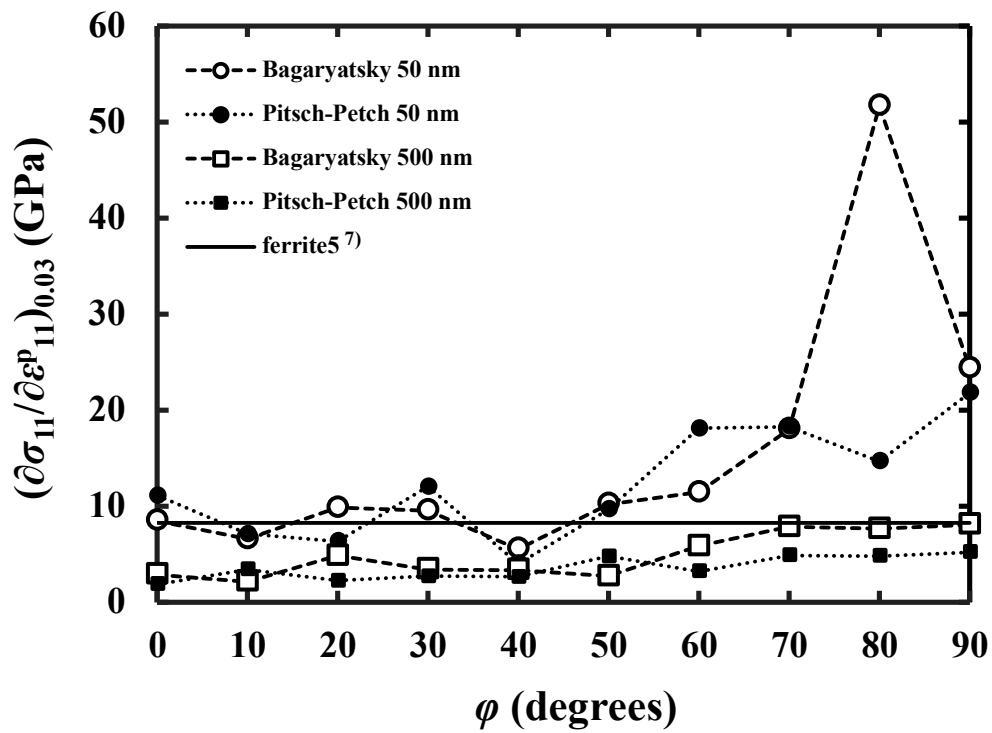
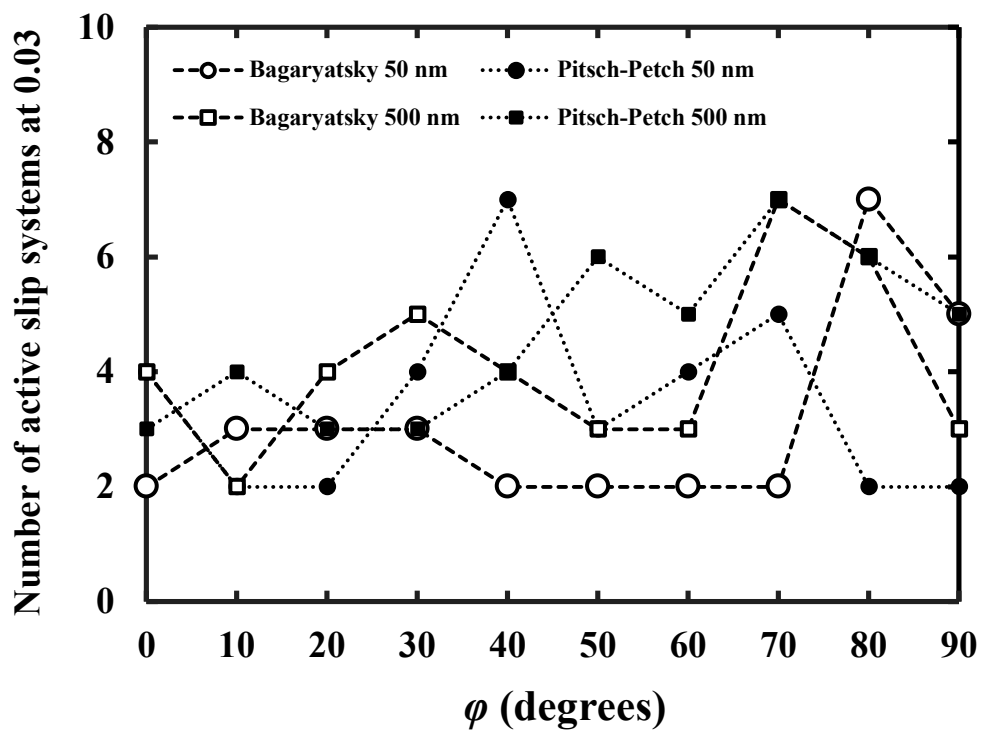
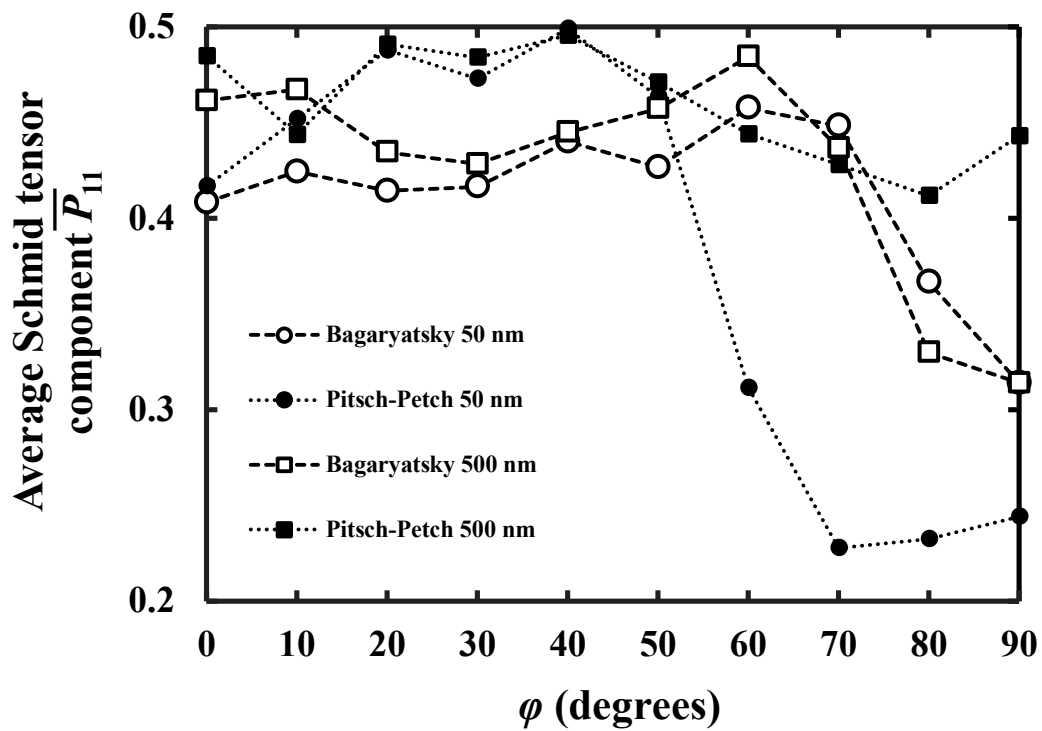


Fig. 4 Loading-direction dependence of the strain-hardening rate of ferrite layer in the pearlite microstructure models when the plastic strain is 0.03.

(a)



(b)



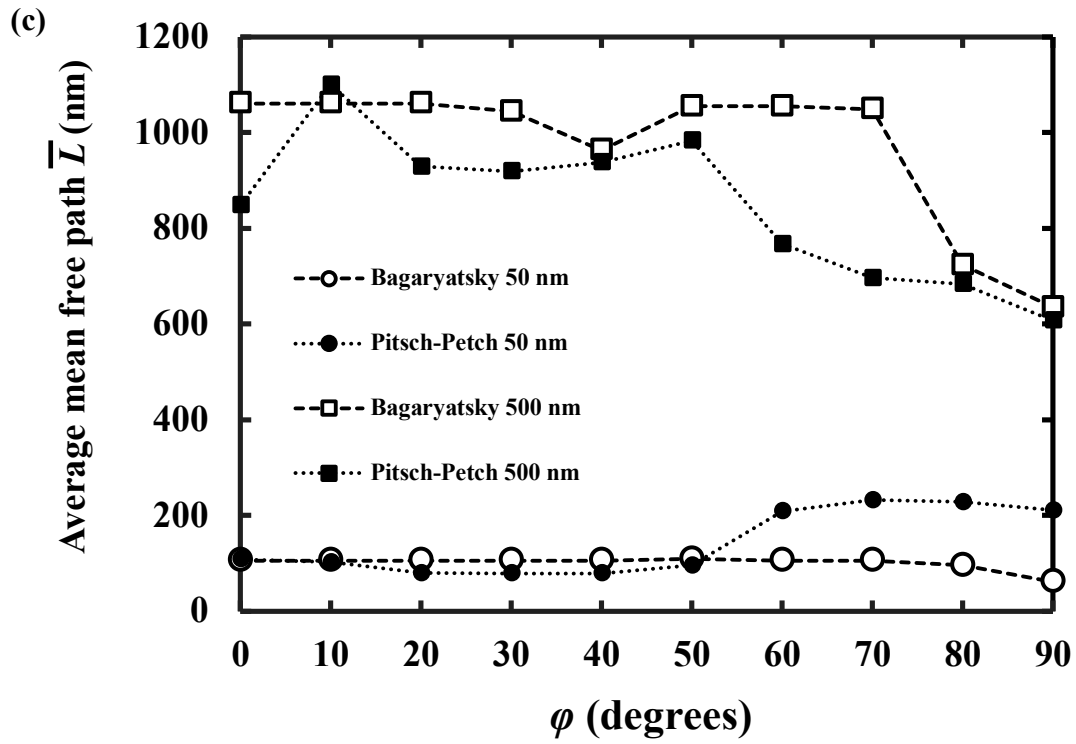


Fig. 5 Dependences of (a) number of active slip systems, (b) average Schmid tensor component, and (c) average MFP on strain-hardening rate of ferrite layer in the pearlite microstructure models when the plastic strain is 0.03.

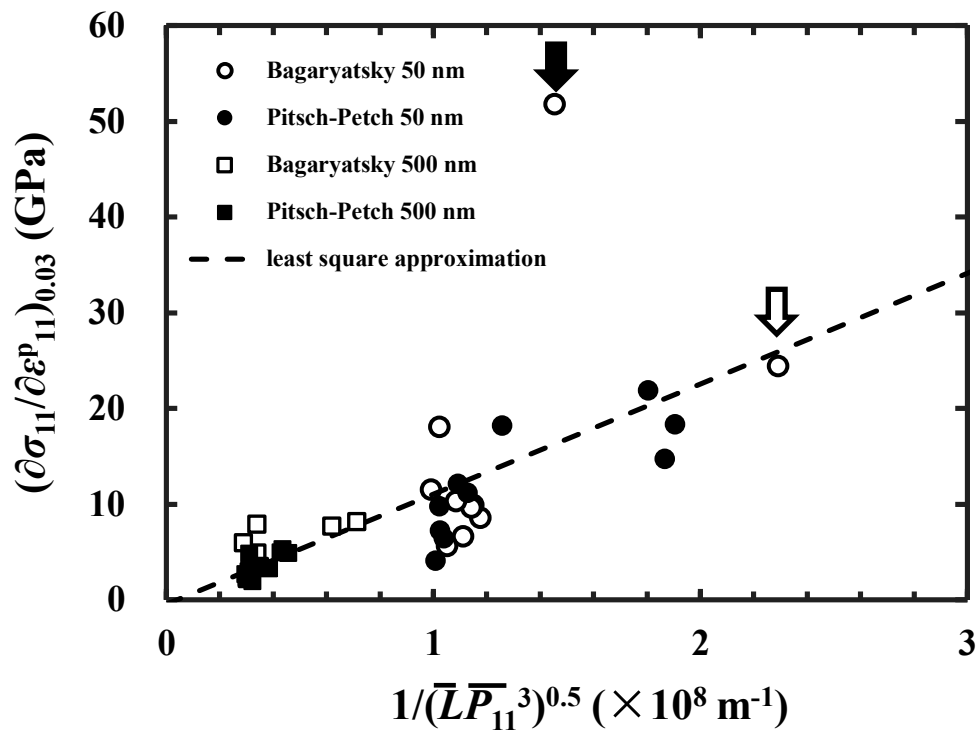


Fig.6 Changes of the strain-hardening rate of ferrite layer in the pearlite microstructure models with  $1/\sqrt{\overline{LP}_{11}^3}$ . The black and white arrows represent the strain-hardening rate of the models with the Bagaryatsky relationship for  $\varphi = 80^\circ$  and  $90^\circ$  when  $d = 50$  nm, respectively.

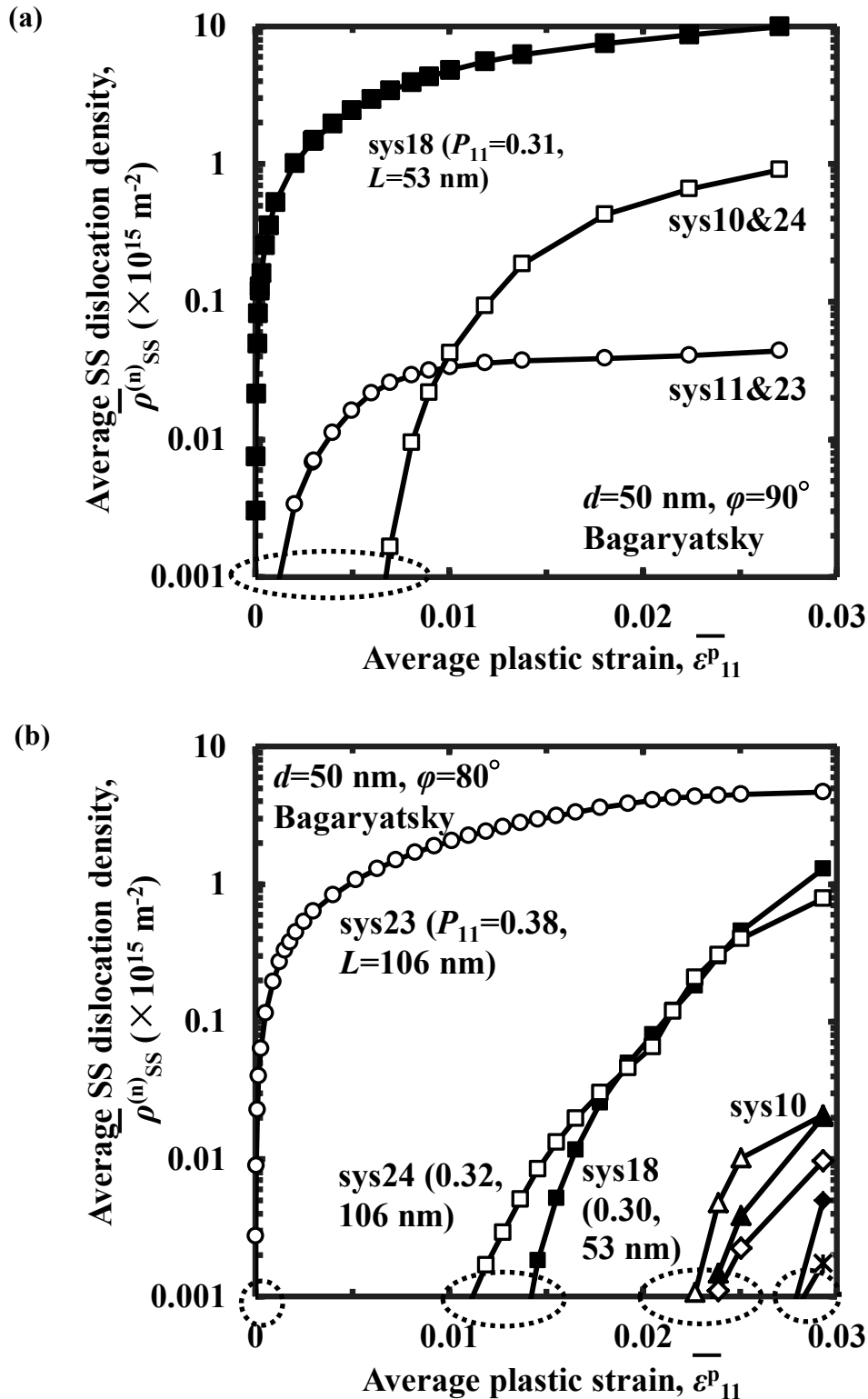


Figure 7. Average SS dislocation density-strain curves for ferrite layer in the pearlite microstructure models with  $d = 50 \text{ nm}$ . (a)  $\varphi = 90^\circ$  and (b)  $\varphi = 80^\circ$ . Crystal orientation relationship is Bagaryatsky. Sys10, 11, 18, 23 and 24 indicate  $(2\ 1\ 1) [-1\ 1\ 1]$ ,  $(1\ 1\ 0) [-1\ 1\ 1]$ ,  $(1\ 1\ 2) [1\ 1\ -1]$ ,  $(1\ 1\ 0) [1\ -1\ 1]$  and  $(1\ 2\ 1) [1\ -1\ 1]$  slip systems, respectively. Numbers in the neighbour bracket show Schmid tensor component and MFP of the slip system, respectively.